Miniaturization Design Study of a Dipole Magnet Applied to Proton Therapy BeamLine

Xuchuan Liang, Yu Chen, Yicheng Liao, Qushan Chen*, Ziyi Yang, Zhenyi Yang, Xu Liu, Bin Qin

State Key Laboratory of Advanced Electromagnetic Technology, School of Electrical and Electronic Engineering, Huazhong University of Science and Technology, WuHan, 430070, HuBei, China[†]

m202472619@hust.edu.cn; yu_chen2000@hust.edu.cn; liaoyicheng@westlake.edu.cn; chenqushan@hust.edu.cn; yang_zi_yi@126.com; m202372453@hust.edu.cn; lxhustliu@hust.edu.cn; bin.qin@hust.edu.cn

Received Day Month Year
Revised Day Month Year
Accepted Day Month Year
Day Month Year

The miniaturization of magnets is crucial for reducing both the physical footprint and the construction cost of a proton therapy facility. The configuration of dipole magnets significantly influences the design of the compact gantry. However, current research demonstrates a degree of subjectivity in achieving an optimal balance between magnet compactness and saturation levels. This study introduces a novel design principle aimed at miniaturizing the yoke of dipole magnets. To be specific, two metrics (i.e. magnet efficiency and magnetization uniformity) are adopted to develop an optimized design that achieves significant weight reduction while maintaining essential magnetic performance characteristics. For the 57-degree dipole magnet discussed in this paper, finite element simulations demonstrate that the optimized design achieves a weight reduction of 39.6% for the yoke (from 5.38 to 3.24 tons) while maintaining transverse and integrated field homogeneity within the stringent ±0.05% tolerance threshold, and exhibits satisfactory excitation linearity. The design of this study can provide insight for the subsequent construction of a compact gantry.

Keywords: Compact accelerator magnet; dipole magnet optimization; field homogeneity control.

1. Introduction

Proton therapy has emerged as a promising treatment modality for various types of cancer, using the unique physical properties of protons to deliver precise doses of radiation to tumors with minimal damage to surrounding healthy tissues.[1] Accord-

---

[*] Corresponding author.

[†] This work was supported by the National Natural Science Foundation of China (No.11975107, 12205111) and the National Key Research and Development Program of China (No. 2016YFC0105305)

ing to the statistics of the Particle Therapy Co-operative Group (PTCOG), there are currently 119 proton therapy centers in operation globally.[2]

Despite the relatively mature state of proton therapy technology, its widespread adoption remains constrained by high manufacturing costs and substantial spatial requirements. To enhance its applicability, current development efforts focus primarily on device miniaturization and increasing the radiation dose rate.[3–5] Recent reports on FLASH effects of ultrahigh dose rate have further highlighted the potential of increasing dose rate to eradicate tumor cells effectively while significantly reducing toxicity to surrounding healthy tissues.[6,7] However, existing proton therapy systems typically operate at a dose rate below 3 Gy/min, which is substantially lower than the dose rate of 40 to 100 Gy/s associated with FLASH radiotherapy.[8] In light of these challenges, there is a pressing need for compact and efficient treatment facilities capable of accommodating an increasing patient load while maintaining high quality of treatment .[9]

One of the key components of a proton therapy facility is the gantry, a rotating structure that transports the proton beam from various angles around the patient. Current gantry-less proton therapy facilities are primarily utilized for treating small-volume tumors in the head and neck region,[10,11] the ocular area,[12] and the sinonasal cavity.[13] However, broader application of these systems is limited by several factors: The treatment chair is less flexible than a gantry in terms of achievable irradiation angles, restricting its use to specific treatment sites. For instance, the posterior-oblique incidence required for prostate cancer treatment to spare the rectum and bladder is more easily achievable with a rotating gantry;[14] seat positioning poses challenges to patient comfort and stability, especially for frail or disabled individuals who cannot maintain the required posture for extended periods, increasing the risk of intrafraction motion;[15] and the technology itself is still in the phase of early promotion and clinical validation. These limitations highlight the essential role of rotating gantries, which enable multiangle irradiation and facilitate stable supine positioning, thereby improving treatment precision and expanding the range of treatable tumor sites.

Conventional gantries are often large and heavy, presenting significant challenges in terms of installation, operational costs, and patient accessibility.[16] Consequently, the design of compact gantries has become a hot issue in modern proton therapy facilities with the aim of reducing both the physical footprint and the overall weight of the system.

The Gantry 2 at Paul Scherrer Institute (PSI/Switzerland) represents one of the earliest implementations of proton pencil-beam scanning (PBS) technology in rotating gantry configurations.[17] Using an upstream scanning mode that generates a lower skin dose,[18] this system allows a reduced gantry radius. Similarly, the ProteusOne gantry of Ion Beam Applications (IBA/Belgium) employs upstream scanning and features a 220-degree rotational gantry combined with a 180-degree treatment couch, effectively decreasing the footprint of the equipment.[19]

In addition to innovative gantry layout designs,[20–22] the integration of superconducting (SC) magnets has shown significant promise for achieving compactness.[5] SC magnets can excite strong magnetic fields while occupying substantially less space than normal-conducting (NC) magnets. However, the implementation of SC technology presents several design challenges, including slow ramping rates,[23] quench protection,[24] and thermal management issues.[25] These challenges may hinder the operational efficiency of SC gantries, particularly in dynamic treatment scenarios that require rapid adjustments to the magnetic field.

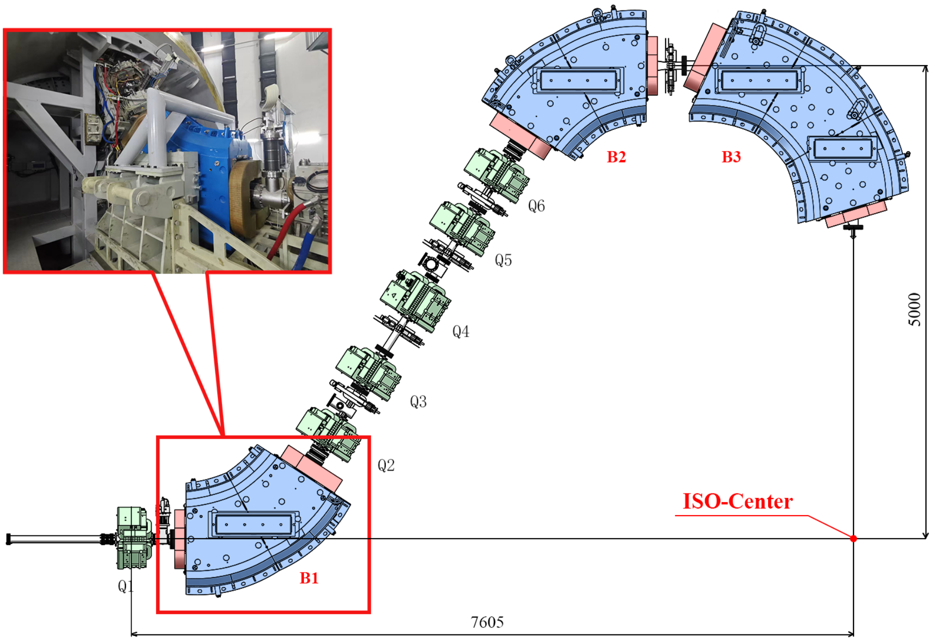

Fig. 1: Layout of the HUST-PTF gantry beamline with a photographic image of the 57-degree bending dipole magnet on site.

In light of these challenges, investigating the miniaturization design of NC magnets as an effective means to enhance the compactness of gantry systems presents significant research value. Although the basic design theory for NC magnets has advanced considerably in previous studies, substantial challenges remain. The primary difficulty lies in achieving an optimal balance between magnet compactness and an acceptable saturation level.[19] Current research in this field often exhibits a degree of subjectivity due to the absence of a systematic method for evaluating whether miniaturization designs have achieved optimal performance.

Huazhong University of Science and Technology is currently constructing a proton therapy facility (HUST-PTF).[26] Fig. 1 shows the layout of the gantry beamline,[27] which contains two 57-degree dipoles (B1 and B2) and a 90-degree dipole (B3). Different from the PSI Gantry 2 system and ProteusOne gantry mentioned previously, the gantry of HUST-PTF adopts the downstream scanning mode, which can adapt to treatment scenarios with higher precision requirements and has much lower requirements for the size of the treatment window of the last dipole magnets.[19,28,29] However, the current yoke configuration of HUST-PTF still shows substantial potential for structural optimization. For example, the yoke of the 57-degree dipole magnet weighs 5.38 tons, which is approaching the design limit of 6 tons for the total weight, including the coil components. Therefore, the miniaturization of dipole magnets is crucial to reduce the footprint of the gantry and enhance rotational flexibility.

The Shanghai Advanced Proton Therapy (SAPT) project enhances the field intensities of the dipole magnets to achieve a smaller bending radius, thereby reducing the external radius of the rotating gantry. This optimization resulted in weight reductions of 410 kg and 550 kg for the 60-degree and 90-degree dipole magnets, respectively.[30] However, this approach requires major modifications to the gantry structure, which may be not suitable in some custom occasions.

The European Organization for Nuclear Research (CERN) has developed a compact and rapidly adjustable FeCo dipole magnet prototype for medical gantry systems. This prototype utilizes high-saturation FeCo alloy laminations (2.35T) and optimized cooling-coil integration, achieving a 30% reduction in yoke size compared to conventional FeSi-based designs, making it highly suitable for dynamic beam steering in compact hadron therapy facilities.[31]

In the European High Field Magnet (HFM) program, a systematic study on Nb_3Sn-based Short Model Coil (SMC) dipole magnets revealed a nonlinear coupling relationship between the yoke and shell thickness: when the yoke thickness is below 55 mm, the system rigidity is significantly enhanced, allowing for the use of thinner shells; beyond this threshold, pre-stress becomes dominated by the shell thickness and assembly interference.[32] Although the study focuses on superconducting magnets, its analytical framework emphasizing the relationship of structural geometric parameters provides a valuable reference for our research.

Therefore, this study proposes a new design method for the miniaturization of NC magnets, specifically for the 57 - degree dipole in the HUST-PTF gantry. This approach involves a comprehensive evaluation of the geometric parameter ratios through a comparative analysis of two key metrics: magnet efficiency and magnetization uniformity, which are crucial for achieving optimal performance in compact designs.

The challenges faced by this optimization approach stem from the design requirements of the HUST-PTF beamline. The beamline is designed to bend proton beams within an energy selection range of 70 to 240 MeV,[33] corresponding to a magnetic rigidity variation of 1.20 to 2.37 T·m. With a nominal bending radius of 1.5 m, the maximum field is 1.58 T.[34] However, the selected iron core material,

Table 1: Main parameters of the 57-degree dipole[29]

Parameter	Specification
Yoke structure	H type
Pole gap	63 mm
Bending angle	57-degree
Bending radius	1500 mm
Magnetic field range	0.80 T-1.58 T
good-field region	H ±35 mm × V ±26 mm
Transverse field homogeneity	$\leq \pm 0.05\%$
Integrated field homogeneity	$\leq \pm 0.05\%$
High order harmonic errors	$\leq \pm 0.05\%$

B50AS silicon steel laminations, exhibits the initiation of magnetic saturation at 1.4 T. Thus, the inevitable problem of yoke saturation poses a design challenge.

Another critical consideration in optimization design is the quality of the magnetic field, which must be maintained while improving the compactness of the magnet. For instance, field homogeneity and harmonic errors should be maintained within the limits of ±0.05% throughout the operational range according to Table 1. To achieve this precision requirement, detailed pole contour shimming and iterative optimization of pole end chamfering are implemented to reduce the effect of fringe field. These multistage strategies ensure that the miniaturized magnet achieves magnetic performance comparable to that of the existing dipole magnet in the HUST-PTF.

The remainder of this study is organized as follows: Section II introduces the selection of key parameters for the two-dimensional cross section based on a quantitative evaluation of saturation, as well as the optimization of pole contour shimming. Section III presents the iteration of pole end chamfering following the setup of the three-dimensional model, along with a comparison of magnetic field performance to that of the original dipole magnet, and extended the implementation of the proposed optimization strategy to the 90-degree dipole. Finally, Section IV summarizes the conclusions that are of reference value in the design process. For simulation and iterative optimization, SOLIDWORKS is utilized for modeling, while magnetic field evaluation is performed with OPERA.[35]

2. 2D Transverse cross section Optimization

This section aims to achieve an optimal level of miniaturization for the two-dimensional cross section, which determines the overall volume of the dipole magnet. Following the establishment of the two-dimensional cross section, the transverse field homogeneity is optimized through pole contour shimming.

2.1. *Saturation Quantitative Evaluation Method*

The two-dimensional cross sectional configuration of the dipole magnet mainly includes the yoke and the coil cross section. The coil cross sectional configuration is 150 mm × 90 mm with a maximum operation current density of 4.5 $\mathrm{A/mm^2}$.[29] The copper conductor featuring a cross section of 12 mm × 12 mm with a cooling hole of ϕ 6 mm is selected. A rough thermal analysis indicates that the maximum increase in temperature would be less than 20 °C under a cooling pressure of 10 bars. Consequently, the design focus shifts to the dimensional optimization of the yoke thickness T_{yoke} and the pole width W_{pole} (Fig. 3). For H-type dipole magnets, the proportionality coefficient is defined as

$$\delta = \frac{2T_{\text{yoke}}}{W_{\text{pole}}}, \tag{1}$$

In the design of dipole magnets, δ is typically chosen within the range of 1.05 to 1.3. To determine the optimal coefficient δ, a systematic evaluation of the saturation conditions of the magnetic yoke under various cross sectional configurations corresponding to varying values of δ is required.

To be specific, when the magnet achieves optimal compactness, the corresponding value of δ should exhibit the following characteristics: first and foremost, the saturation level of the magnet should remain within an acceptable range when the magnetic field in the pole gap reaches its maximum. Moreover, the magnetization across different parts of the magnet should be as uniform as possible, indicating the effective utilization of the magnetization capacity of the ferromagnetic material. The average saturation level of the magnetic yoke can be quantified by magnet efficiency, which is defined as[36]

$$\xi_{\text{exc}} = \frac{NI_{\text{gap}}}{NI_{\text{total}}}, \tag{2}$$

where NI_{total} represents the total excitation current, which consists of two components: NI_{gap}, which is required to establish the magnetic field in the gap, and NI_{yoke}, which accounts for the magnetomotive force needed to magnetize the ferromagnetic yoke. These components can be determined by integrating the magnetic field along the yoke and the pole gap, respectively.

In conventional H-type dipole magnet structures, the integral path length L along the magnetic yoke and the height h of the pole gap satisfy the geometric relationship $L \geq 10h$. Under unsaturated conditions with permeability $\mu \geq 1000$, it can be approximated that $\xi_{\text{exc}} \geq 99\%$.[36] Consequently, under high-field conditions, the decrease in permeability μ results in a reduction of ξ_{exc}. Therefore, the preliminary comparison approach is to analyze the changing trend of ξ_{exc} for each cross sectional configuration under different values of δ.

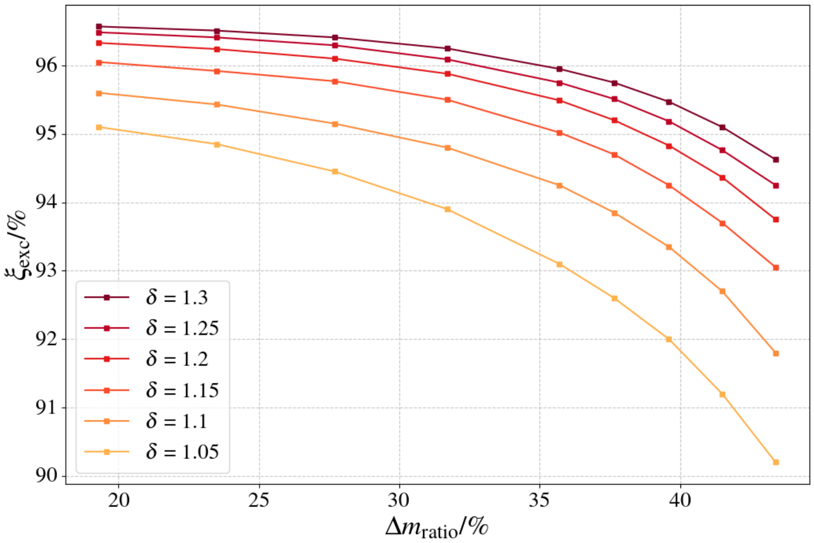

Fig. 2: The relationship between ξ_{exc} and $\Delta m_{\mathrm{ratio}}$ with different values of δ.

The weight reduction ratio of the magnet $\Delta m_{\mathrm{ratio}}$ is defined as the proportion of mass saved by the miniaturized design relative to the mass of the existing dipole magnet. Fig. 2 shows the relationship between ξ_{exc} and $\Delta m_{\mathrm{ratio}}$. A higher value of δ is associated with an increase in ξ_{exc} at the same $\Delta m_{\mathrm{ratio}}$; however, this does not imply enhanced saturation performance. As illustrated in Fig. 3, high-δ configurations exhibit significant magnetization discrepancies between poles and yokes. To be specific, at $\xi_{\mathrm{exc}} = 95\%$, the poles experience severe saturation ($B_{\mathrm{pole}} > 2.0$ T), while the yokes remain under-saturated ($B_{\mathrm{yoke}} < 1.3$ T). This non-uniform magnetization violates the design objectives. In contrast, lower δ values enhance magnetization uniformity but limit the potential for weight reduction.

Therefore, to obtain the optimal value of δ, it is necessary to introduce another metric to quantitatively assess the uniformity of magnetization. As shown in Fig. 3, the central axis of the half-side yoke section is selected as the measurement path. The magnetization uniformity factor can be calculated as

$$U_{\mathrm{mag}} = \frac{1}{1 + \left| \frac{\Delta\mu}{\overline{\mu}} \right|}, \tag{3}$$

where $\Delta\mu$ is the difference between the maximum and minimum permeability and $\overline{\mu}$ is the average permeability along the measurement path. The factor U_{mag} is normalized to the interval (0, 1), higher values of which reflect better magnetic homogeneity.

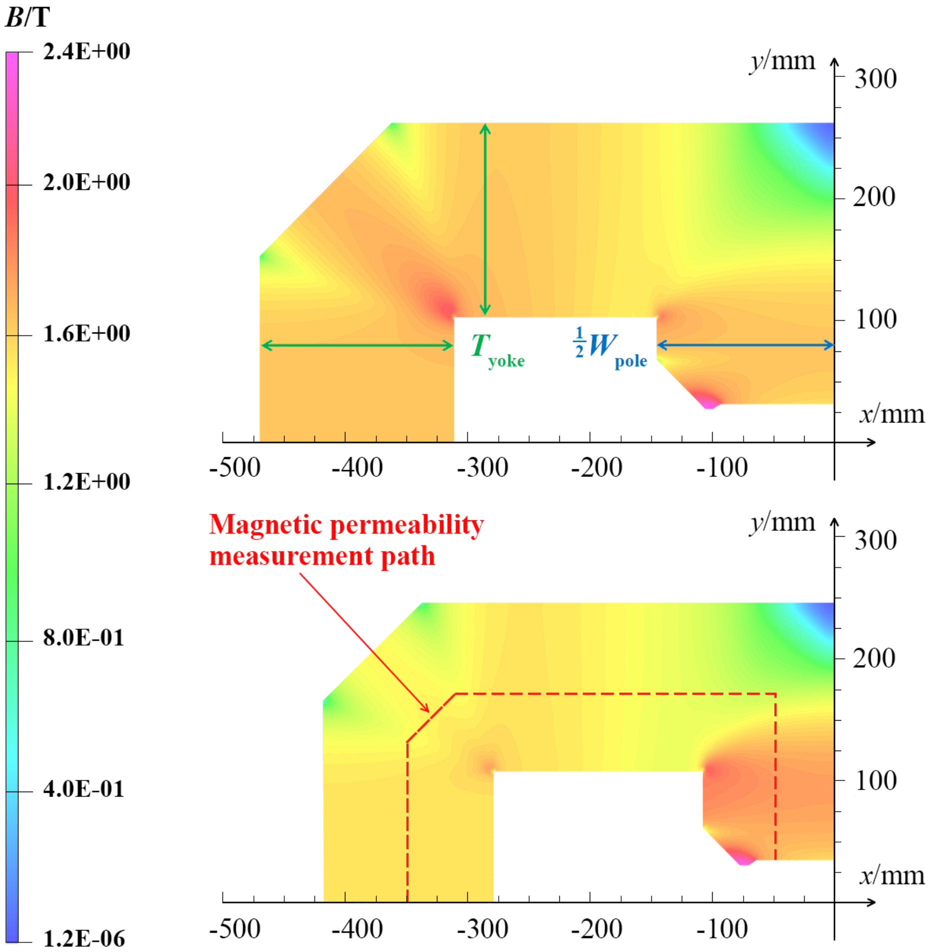

Fig. 3: 2D magnetic field distributions at field of 1.58 T and $\xi_{\text{exc}} = 95\%$ with $\delta = 1.05$ (above) and $\delta = 1.3$ (below) configuration.

Simulations were performed on dipole magnet configurations with varying δ values. For each δ, at least five simulations corresponding to different Δm_{ratio} were performed. The relationship between $\overline{\mu}$ and ξ_{exc} is calculated for each set and plotted in a single graph, as shown in Fig. 4. The resulting $\overline{\mu}$ - ξ_{exc} data points corresponding to different δ values almost collapsed onto a single curve, indicating that this relationship between $\overline{\mu}$ and ξ_{exc} is independent of the magnet's geometric shape. Consequently, when ξ_{exc} is the same, the variation in U_{mag} is determined only by $\Delta\mu$ according to Eq. (3).

This allows for a quantitative assessment of internal magnetization uniformity by comparing U_{mag} at a given ξ_{exc}. To ensure adequate excitation linearity at high fields, ξ_{exc} should be maintained above 95%. Therefore, the subsequent design ap-

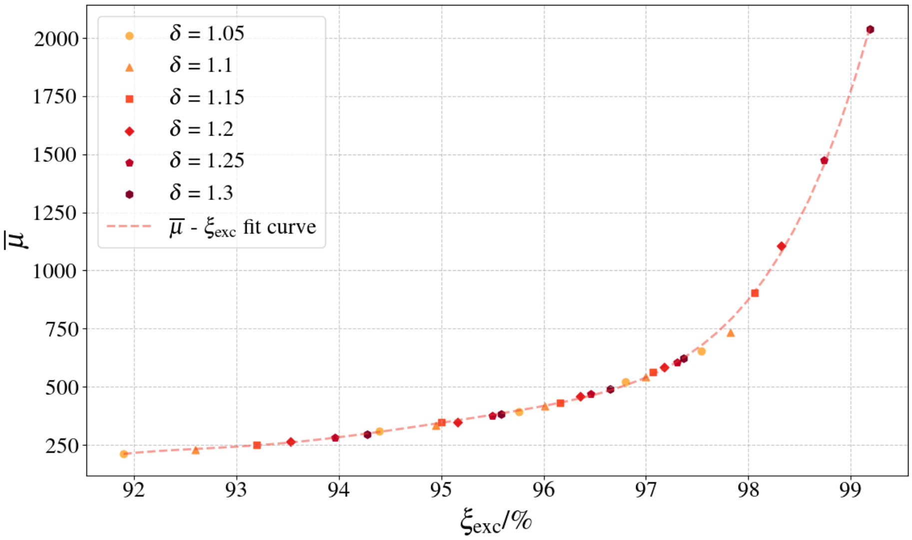

Fig. 4: The mapping between $\overline{\mu}$ and ξ_{exc} with varying δ values.

proach involves comparing Δm_{ratio} and U_{mag}, selecting the optimal configuration at $\xi_{\text{exc}} = 95\%$ across different δ for dipole magnets.

Fig. 5 illustrates the changing trends of ξ_{exc} and U_{mag} with respect to Δm_{ratio} for different δ. In each figure, the vertical and horizontal dashed lines indicate the values of Δm_{ratio} and U_{mag} at $\xi_{\text{exc}} = 95\%$, respectively. Consequently, the shape of the shaded region can be used to compare the overall levels of U_{mag} and Δm_{ratio}. Notably, the optimal performance is observed at $\delta = 1.15$ [Fig. 5 (c)], which produces a uniformity factor of $U_{\text{mag}} = 0.76$ (corresponding to a relative permeability deviation within 100) along with a weight reduction of 35.7%. Decreasing δ improves U_{mag} but significantly reduces Δm_{ratio}, and increasing δ beyond 1.15 leads to a rapid degradation of U_{mag}. Therefore, the optimal ratio δ should be selected in the vicinity of 1.15.

Based on the results presented above, the final design adopts a pole width of $W_{\text{pole}} = 220$ mm and a yoke thickness of $T_{\text{yoke}} = 126.5$ mm, as illustrated in Fig. 6. Compared to the original HUST-PTF dipole magnet design, which features $W_{\text{pole}} = 280$ mm and $T_{\text{yoke}} = 170$ mm ,[34] this configuration achieves an approximate 40% reduction in the weight of the dipole magnet, amounting to approximately 2150 kg.

This design methodology yields a generalizable insight: If more advanced ferromagnetic materials with higher saturation thresholds are available, larger δ can be selected to enhance Δm_{ratio} and reduce magnet size without inducing pole saturation. Conversely, if minimizing weight is not the primary objective, a smaller δ should be chosen to maximize magnetization uniformity and prevent saturation. This systematic approach provides clear guidance for balancing magnet compact-

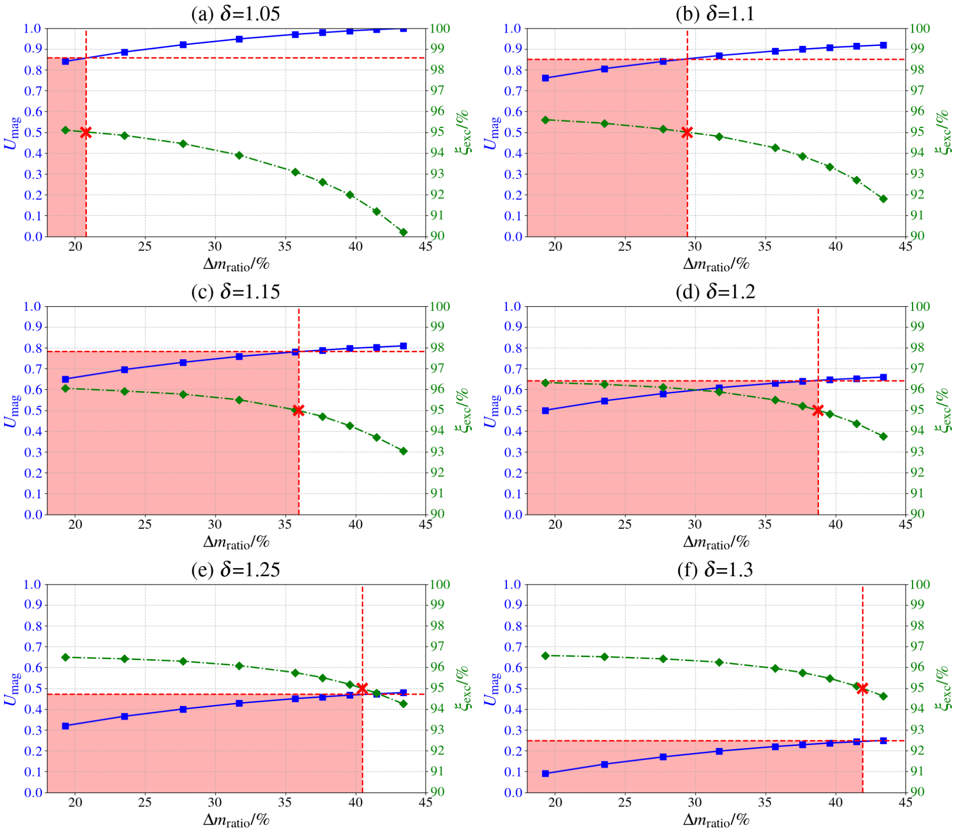

Fig. 5: The changing trends of magnet efficiency ξ_{exc} and magnetization uniformity U_{mag} versus weight reduction ratio Δm_{ratio} with different values of δ. The red shaded area serves as a comparison, illustrating the comprehensive performance of U_{mag} and Δm_{ratio} when $\xi_{exc} = 95\%$.

ness and magnetic field performance.

2.2. *Pole Contour Shimming Optimization*

Pole contour shimming is employed to optimize transverse field homogeneity. The trapezoidal shimming method is selected for its favorable balance between manufacturing precision and cost effectiveness in this design. This approach involves the iterative optimization of three key geometric parameters: the thickness of the shim a, the width of the shim b, and the bevel angle c, as illustrated in Fig. 6.

The principle of pole contour shimming involves shortening the magnetic flux leakage path at the magnet edges, thereby compensating for the field attenuation caused by fringe field effects.[36] As shown in Fig. 7, which presents the transverse distribution of the magnetic field in the center plane of the good-field region, the

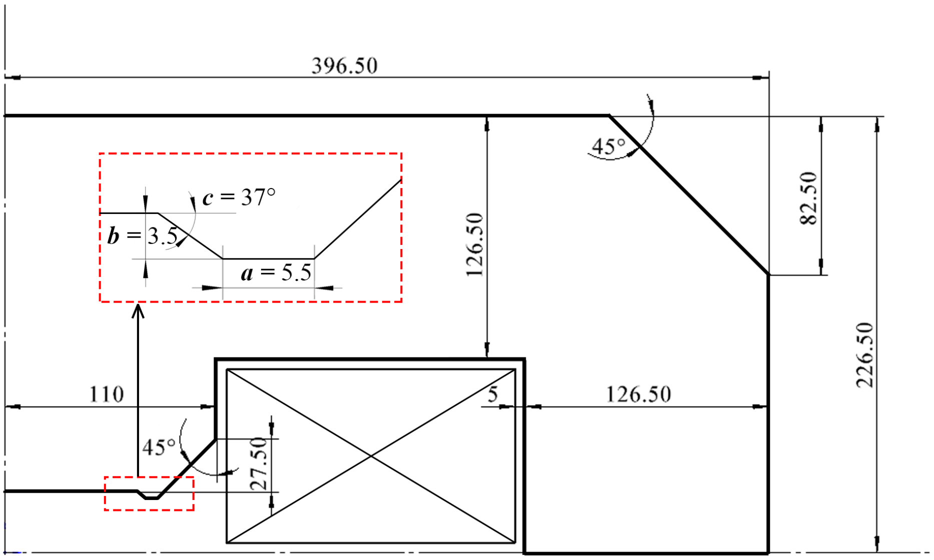

Fig. 6: Optimized 2D cross sectional design with annotated key geometric parameters of trapezoidal shimming method.(unit: mm)

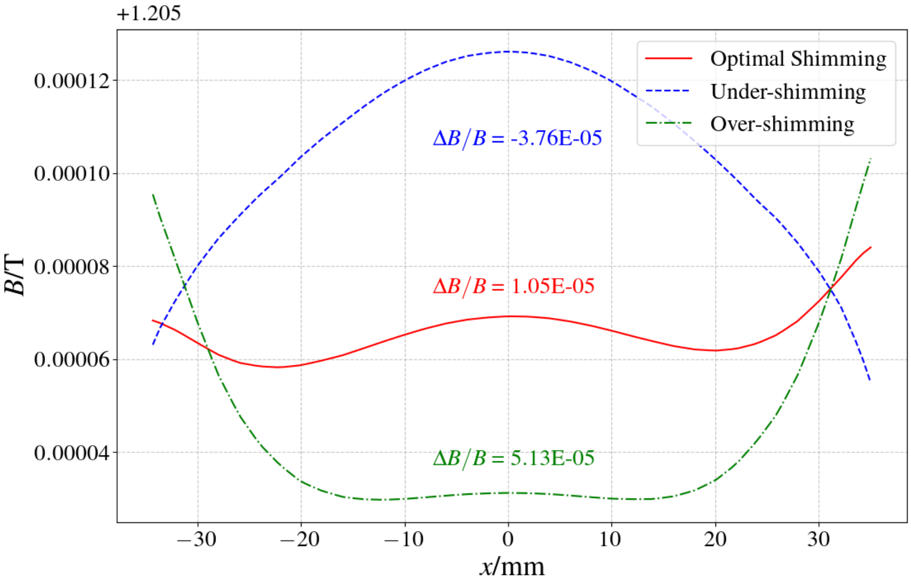

Fig. 7: Transverse distribution of magnetic field in the center plane of good-field region with optimal shimming, under-shimming, and over-shimming configuration.

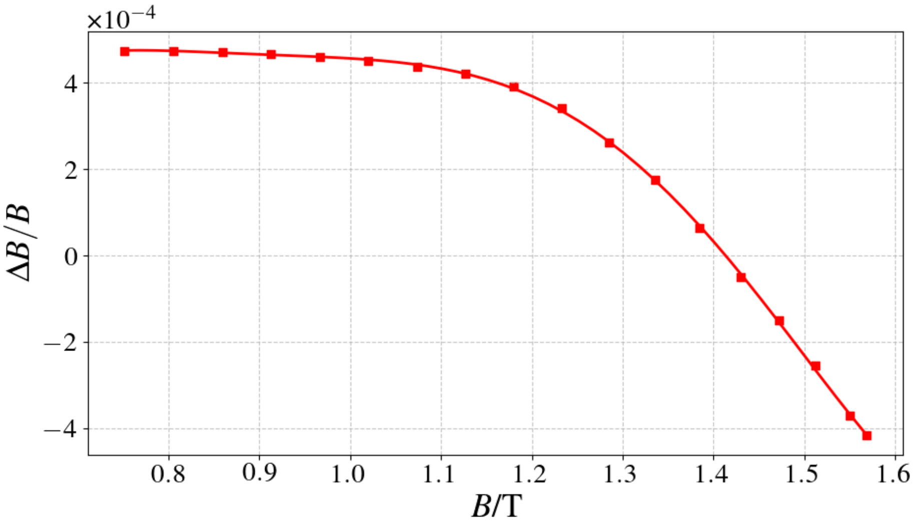

Fig. 8: Transverse field homogeneity distribution across the operating field range.

optimal shimming configuration yields a characteristic W-shaped field profile, indicative of high field uniformity. In contrast, over-shimming leads to a convex field distribution, while under-shimming results in a concave profile, both of which deviate from the desired uniformity.

To achieve uniform transverse field homogeneity across the entire operational field range, the shim geometry is specifically tuned to create a slightly convex profile at maximum field strength and a concave profile at minimum field strength. This optimization strategy ensures that during intermediate field operation (the most frequent operational state), the field distribution naturally evolves into the desired W-shaped profile due to the enhanced fringe field effects as the magnetic field increases.

Notably, there are multiple viable shimming solutions for the pole contour optimization. The shimming configuration illustrated in Fig. 6 represents a set of local optima identified through iterative parametric optimization using finite-element analysis. Fig. 8 demonstrates that under the proposed transverse cross section configuration, the transverse homogeneity is constrained within ±0.05% across the operational field range.

3. 3D Field Optimization

Based on the cross sectional design from the previous section, three-dimensional modeling is conducted, followed by optimization of the integral field. This section subsequently presents a comparison between the optimized and initial designs in terms of magnetic field performance and excitation linearity. To validate the general applicability of the optimization strategy, similar optimization is performed

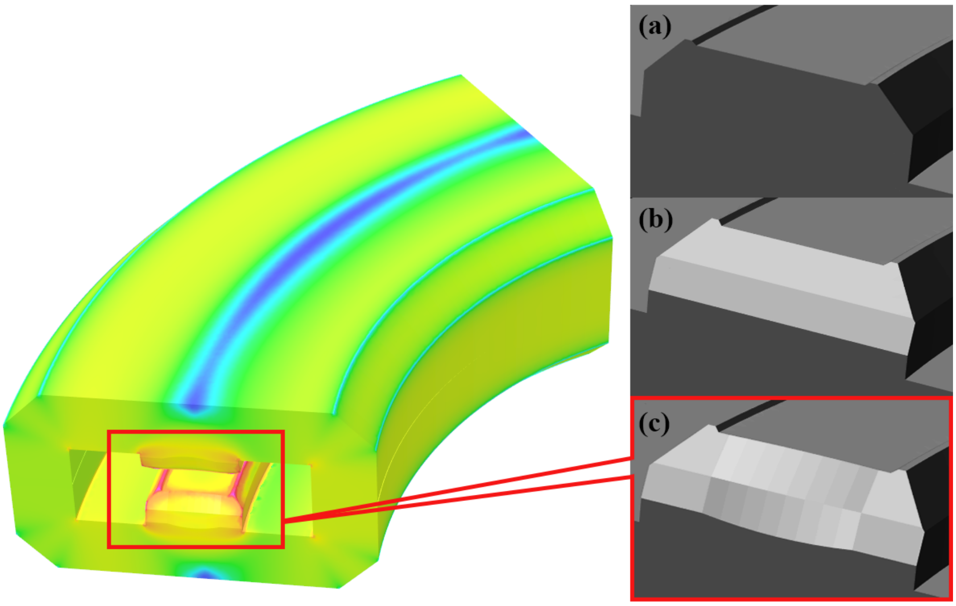

Fig. 9: Schematic diagrams of end chamfering configurations: (a) unchamfered initial end profile; (b) linear chamfered profile for saturation reduction and effective bending angle adjustment; (c) curvilinear chamfered profile with polygonal approximation to reduce multipole errors.

on the 90-degree dipole magnet, with a comparative analysis of the integral field distributions for both the 57-degree and 90-degree dipole magnets.

3.1. *Pole End Chamfering for Integral Field Optimization*

After performing a Fourier harmonic analysis of the three-dimensional integral field, iterative optimization is required for two components: the effective bending angle calculated from the dipole moment and the higher-order harmonic errors.[37]

Due to fringe field effects, the effective magnetic length of the dipole exceeds its mechanical pole length. Therefore, the mechanical pole angle is intentionally designed to be slightly smaller than the effective bending angle of 57-degree. By iterative optimization of the linear chamfering, the effective bending angle is not only precisely calibrated to 57-degree, but the saturation of the pole end is also reduced. As shown in Fig. 9 (b), the linear chamfering profile adopts a three-segment polyline approximation in place of the theoretically ideal Rogowski curve to improve manufacturability.[38]

Subsequently, the high-order harmonic errors are analyzed at several typical levels within the operating field range. The data presented in Table 2 lead to the following conclusions:

Table 2: Integral Field Harmonic Components Before Optimization (×0.01%)

B_1 (T)	$\frac{B_2}{B_1}$	$\frac{B_3}{B_1}$	$\frac{B_4}{B_1}$	$\frac{B_5}{B_1}$	$\frac{B_6}{B_1}$	$\frac{B_7}{B_1}$
0.80	-3.85	0.79	-0.04	3.49	0.28	2.35
1.00	-3.79	0.28	-0.06	3.19	0.29	2.20
1.20	-3.71	-1.45	-0.01	1.92	0.31	1.57
1.40	-3.56	-6.06	0.07	-1.01	0.35	0.11
1.58	-3.43	-11.27	0.18	-3.25	0.37	-0.92

(1) The primary optimization challenge lies in the suppression of the sextupole component ($n = 3$) in the high field range.
(2) Other harmonic components remain within a ±0.05% amplitude range across the full operating field range, which is a favorable characteristic that should be preserved in subsequent optimization stages.
(3) All harmonic components exhibit monotonic trends with increasing excitation.

Harmonic errors can be adjusted by asymmetric chamfering at the pole ends.[39] To be specific, new 2n-pole components can be introduced into the existing magnetic field by adjusting the pole lengths L, while maintaining the contour of the pole cross section.[40] The corresponding depth of the pole end chamfer $\Delta L_n(x)$ can be calculated as:

$$\Delta L_n(x) = \frac{L}{2n}\frac{B_n}{B_1}\frac{\mathrm{Im}\,(x+iy_0)^n}{x_0^{n-1}y_0} \tag{4}$$

where x_0 is the half-width of the good-field region and y_0 is the half-length of the pole gap. The curvilinear chamfer described by Eq. (4) introduces a uniform shift in the relevant harmonic components throughout the operating field range. This is because the chamfer essentially superimposes a higher-order harmonic rather than eliminating it. Consequently, achieving complete harmonic cancelation throughout the entire operating field range is not feasible. Given that the harmonics exhibit a monotonic variation within this range, a feasible strategy is to optimize the sextupole component at both the maximum and minimum fields, corresponding to the upper and lower limits of the allowable precision. This approach ensures that the harmonic errors remain within the specified precision limits throughout the operating field range.

To facilitate iterative optimization and reduce processing complexity, the required chamfer curve is approximated using a polyline, as illustrated in Fig. 9 (c). The optimized configuration, with a central chamfer depth of 1.6 mm, achieves sextupole components of +0.041% at 0.80 T and -0.043% at 1.58 T. Fig. 10 illustrates the changing trend of harmonic components across the operating field range. The results confirm that the harmonic errors are controlled within the precision requirement of ±5%, demonstrating the effectiveness of the proposed pole end chamfering approach.

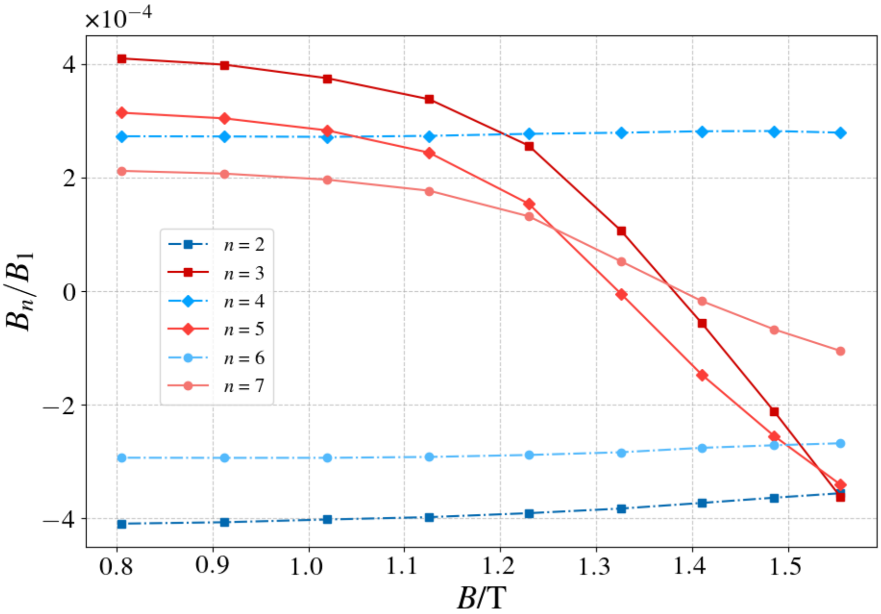

Fig. 10: The changing trends of normalized harmonic components across the operating field range after the pole end chamfering.

The results further reveal that the odd-n harmonics (n = 3, 5, 7, corresponding to the sextupole, decapole, and tetradecapole components), which exhibit geometrically symmetric magnetic field distributions, vary significantly across the operating field range due to the enhanced fringe field effects as the magnetic field increases. In contrast, the even-n harmonics (n = 2, 4, 6, corresponding to the quadrupole, octupole, and duodecapole components) with asymmetric field distributions remain stable throughout the operating range.

These characteristics enable targeted pole end chamfering strategies tailored to different multipole orders. For the odd-n harmonics, the optimization approach described above can be employed. By controlling the harmonics of the maximum and minimum fields, the harmonics can converge within the precision requirement across the entire operating field. Conversely, even-n harmonics can be optimized at a specific field. In an ideal situation, harmonic errors can be optimized to a very low level, potentially eliminating them entirely throughout the operating field range. The chamfer profiles necessary for this purpose can be calculated using Eq. (4) and iteratively optimized to derive a feasible configuration.

3.2. *Magnet Performance After 3D Optimization*

A comparison of the saturation states of the dipole magnet yoke before and after optimization at a maximum field of 1.58 T is presented in Fig. 11, with the same

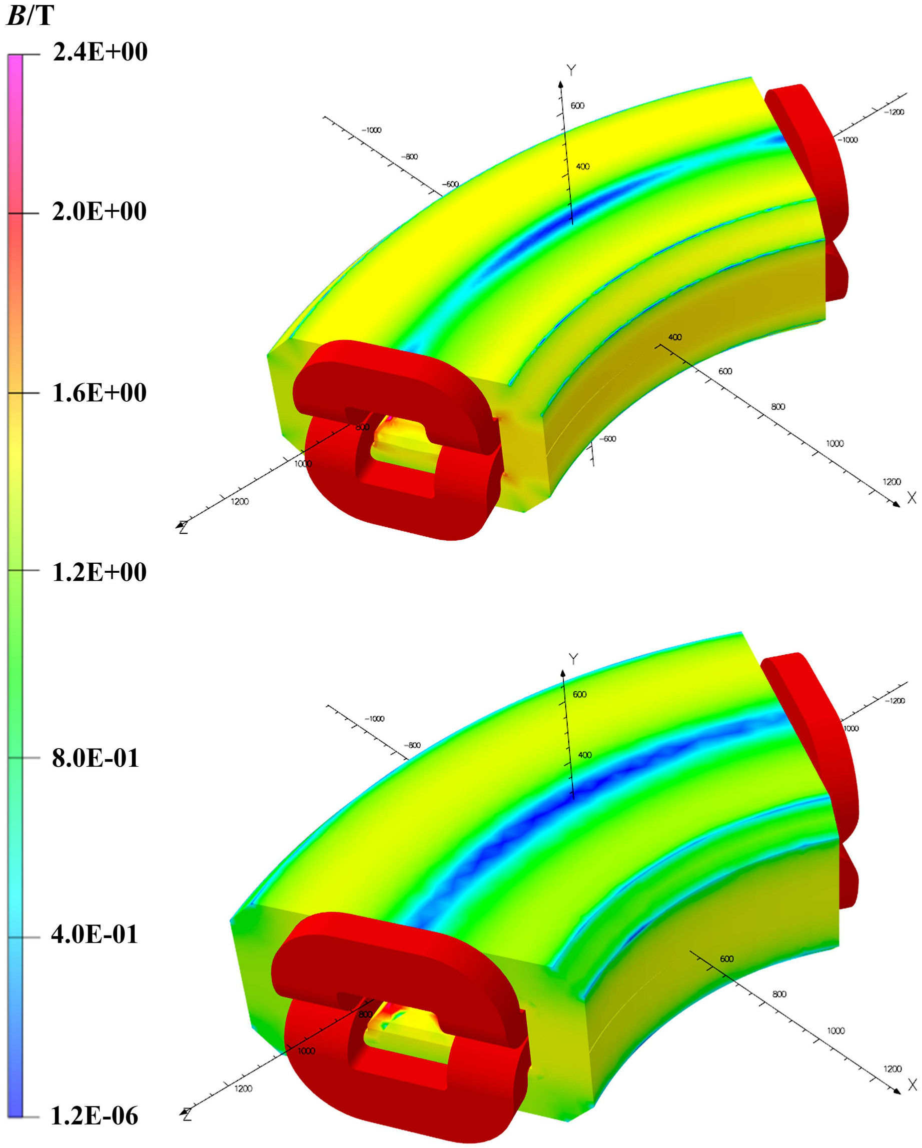

Fig. 11: Comparison of the saturation states of the 57-degree dipole magnet yoke after (above) and before (below) miniaturization at maximum field of 1.58 T, using the same plotting scale and magnetic field intensity color scale.

plotting scale and magnetic field intensity color scale. The proposed miniaturization design achieves a weight reduction of 39.6% (from 5.16 to 3.12 tons) while maintaining field homogeneity and harmonic errors within precision requirements.

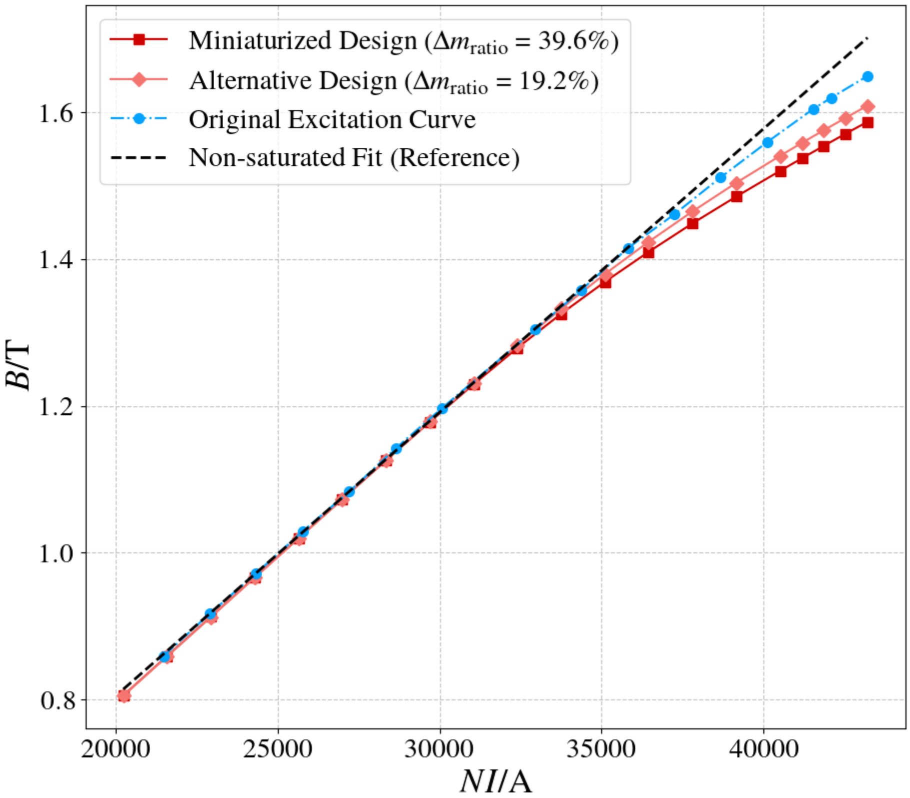

Fig. 12: Comparison of excitation curves for the initial magnet design, compact design, alternative design, and an ideal non-saturated linear fit.

The excitation curves of the original magnet and the miniaturized design are compared in Fig. 12. In the high field range, the increase in saturation levels adversely affects the linearity of excitation. However, within the low to medium field range, which corresponds to the most frequently operating conditions, the linearity remains at a satisfactory level.

Considering the uncertainties in the actual construction and the better performance of the excitation curve, an alternative yoke configuration has been designed. This configuration sacrifices a portion of the weight reduction (19.2%) to achieve an improved excitation linearity, as shown in Fig. 12.

The reduction in linearity at high field regions presents a trade-off between compactness and excitation efficiency, which has minor influence on clinical operations. During beam commissioning, the currents of all magnets on the beamline must be tested and adjusted at each beam energy. As long as the excitation current stays within achievable limits, the terminal beam spot can be optimized accordingly, ensuring that clinical performance is not affected by the field saturation.

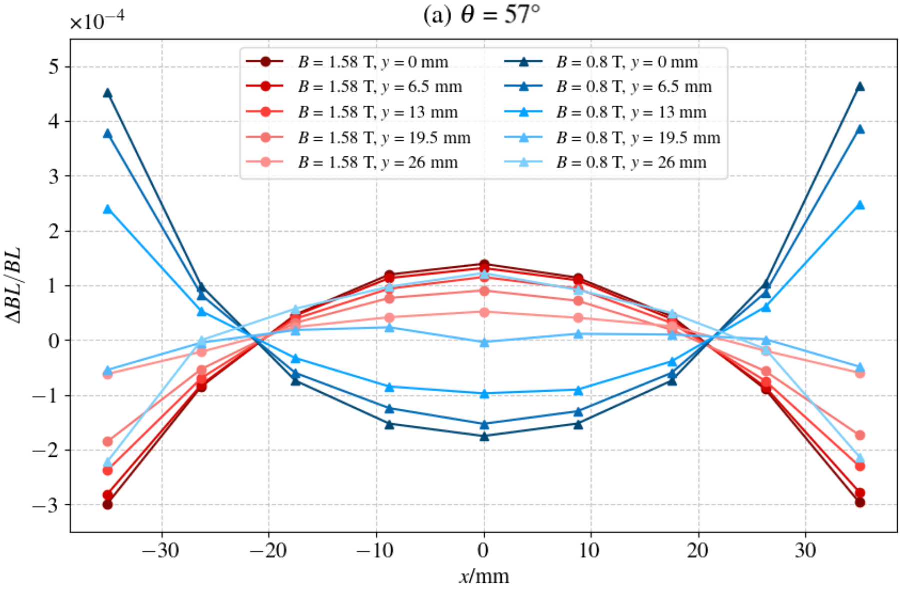

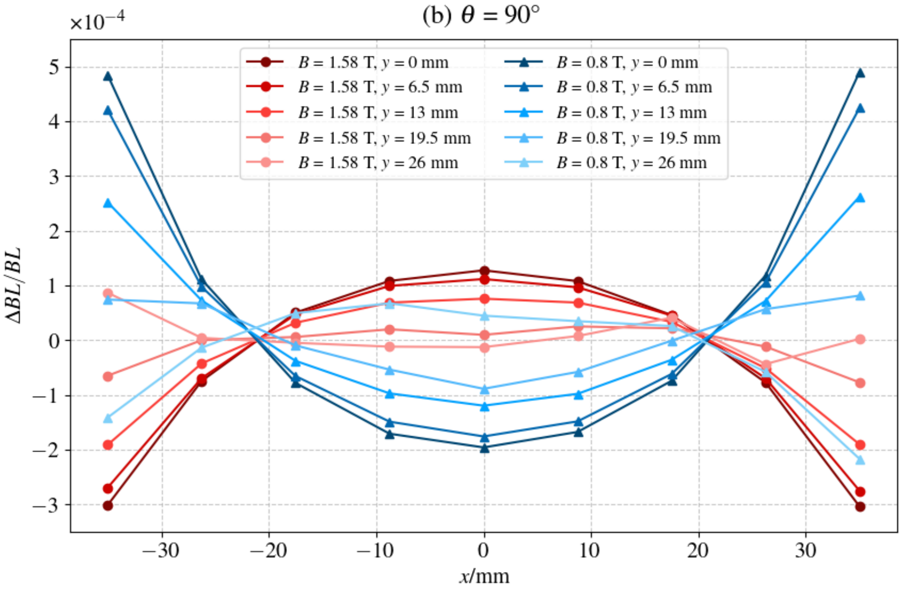

Fig. 13: Integral field uniformity distributions of (a) 57-degree and (b) 90-degree dipole magnets at 0.80 T and 1.58 T. The fields are calculated from $x = -35$ mm to $+35$ mm for planes at $y = 0$, 6.5, 13, 19.5, and 26 mm.

3.3. *Extended Implementation to the 90-degree Dipole*

To validate the general applicability of the proposed method for dipole magnets of similar structure, the optimized cross sectional configuration introduced in Section II is applied to the 90-degree gantry dipole magnet of the HUST-PTF beamline. The pole end chamfering is performed correspondingly following the three-dimensional field optimization strategy detailed in Section III. The final optimized design achieved a Δm_{ratio} of 34.2% compared to the existing magnet. The transverse field homogeneity and harmonic components are maintained within ±0.05%. The integral field uniformity distributions across the entire good - field region for both 57 - degree and 90 - degree dipole magnets at 0.80 T and 1.58 T after three - dimensional optimization are shown in Fig. 13. The results demonstrate that both magnets exhibit similar characteristics in the integral field distribution and satisfy the ±0.05% uniformity requirement across the entire good-field region. These results confirm that the multistage strategy established in previous sections provides a universal optimization paradigm for compact dipole magnet design.

4. Conclusion

This study presents a miniaturization design method for NC dipole magnets, especially for the bending dipoles in the HUST-PTF gantry beamline, including the two-dimensional cross section design of the yoke and the three-dimensional optimization of the pole end. Based on the aforementioned results, the following conclusions are drawn.

(1) A comparative analysis of magnet efficiency and magnetization uniformity, considering saturation levels from both average and uniformity perspectives, determines the optimal thickness of the yoke to half-width of the pole ratio. This optimization resulted in a compact two-dimensional cross section design.

(2) The enhancement of fringe field effects with increasing magnetic field can be utilized for optimizing the transverse field homogeneity. Through iterative optimization of the pole contour shimming, the transverse magnetic field distribution at the maximum and minimum fields exhibits slight convex and concave curves, respectively, enabling the intermediate field distribution to naturally evolve into an ideal W-shaped curve, corresponding to the optimal level of uniformity.

(3) The pole end chamfering optimizes integral field harmonic errors. The fringe field effects exhibit distinct behaviors for odd-n and even-n harmonics due to their differing field symmetries. Optimization of odd-n harmonics, analogous to the approach described in Conclusion 2, requires harmonic control of the maximum and minimum fields to ensure that the harmonics within the operating field converge to the desired precision range. However, even-n harmonic optimization can be achieved at a single field level.

The multistage strategy design presented in this study is applicable to the design of NC magnets with stringent requirements for both the compactness and the performance of the magnetic field. The proposed yoke configuration can also offer valuable insights for the future construction of the compact HUST-PTF gantry.

References

1. W. H. St. Clair, J. A. Adams, M. Bues, B. C. Fullerton, S. La Shell, H. M. Kooy, J. S. Loeffler and N. J. Tarbell, *Int. J. Radiat. Oncol. Biol. Phys.* **58**, 727–734 (2004), `https://doi.org/10.1016/S0360-3016(03)01574-8`.
2. Particle Therapy Co-Operative Group (PTCOG), `https://www.ptcog.site`
3. R. P. Levy, E. A. Blakely, W. T. Chu, G. B. Coutrakon, E. B. Hug, G. Kraft and H. Tsujii, The current status and future directions of heavy charged particle therapy in medicine, in *AIP Conference Proceedings*, Vol. 1099, No. 1 (American Institute of Physics, 2009), pp. 410–425, `https://doi.org/10.1063/1.3120064`.
4. H. Owen, A. Lomax and S. Jolly, *Nucl. Instrum. Methods Phys. Res. A* **809**, 96–104 (2016), `https://doi.org/10.1016/j.nima.2015.08.038`.
5. A. Gerbershagen, C. Calzolaio, D. Meer, St. Sanfilippo and M. Schippers, *Supercond. Sci. Technol.* **29**, 083001 (2016), `https://doi.org/10.1088/0953-2048/29/8/083001`.
6. V. Favaudon, L. Caplier, V. Monceau, F. Pouzoulet, M. Sayarath, C. Fouillade, M.-F. Poupon, I. Brito, Ph. Hupé, J. Bourhis *et al.*, *Sci. Transl. Med.* **6**, 245ra93–245ra93 (2014), `https://doi.org/10.1126/scitranslmed.3008973`.
7. M.-C. Vozenin, P. De Fornel, K. Petersson, V. Favaudon, M. Jaccard, J.-F. Germond, B. Petit, M. Burki, G. Ferrand, D. Patin *et al.*, *Clin. Cancer Res.* **25**, 35–42 (2019), `https://doi.org/10.1158/1078-0432.CCR-17-3375`.
8. J. R. Hughes and J. L. Parsons, *Int. J. Mol. Sci.* **21**, 6492 (2020), `https://doi.org/10.3390/ijms21186492`.
9. J. M. Schippers, A. Lomax, A. Garonna and K. Parodi, Deterministic flow-chart interpretations, in *Proc. Semin. Radiat. Oncol.*, Vol. 28 (Elsevier, 2018), pp. 150–159, `https://doi.org/10.1016/j.semradonc.2017.11.007`.
10. K. Gordon, I. Gulidov, D. Smyk, A. Semenov, K. Golubev, A. Lemaeva, S. Koryakin, E. Jumaniyazova, P. Vishnyakova, I. Eremina *et al.*, *Front. Oncol.* **14**, 1348291 (2024), `https://doi.org/10.3389/fonc.2024.1348291`.
11. A. Beddok, A. Vela, V. Calugaru, T. Tessonnier, J. Kubes, P. Dutheil, A. Gerard, M. Vidal, F. Goudjil, C. Florescu *et al.*, *Radiother. Oncol.* **147**, 30–39 (2020), `https://doi.org/10.1016/j.radonc.2020.03.006`.
12. K. K. Mishra, I. K. Daftari, *Chin. Clin. Oncol.* **5**, No. 4, 50 (2016), `http://dx.doi.org/10.21037/cco.2016.07.06`.
13. K. Gordon, I. Gulidov, D. Smyk, A. Semenov, K. Golubev, A. Lemaeva, S. Koryakin, E. Jumaniyazova, P. Vishnyakova, I. Eremina *et al.*, *Front. Oncol.* **14**, 1348291 (2024), `https://doi.org/10.3389/fonc.2024.1348291`.
14. C. J. Rossi, Jr., *Transl. Cancer Res.* **1**, 173–183 (2012), `https://doi.org/10.3978/j.issn.2218-676X.2012.10.06`.
15. S. Devicienti, L. Strigari, M. D'Andrea, M. Benassi, V. Dimiccoli and M. Portaluri, *J. Exp. Clin. Cancer Res.* **29**, 47 (2010), `https://doi.org/10.1186/1756-9966-29-47`.
16. J. M. Schippers, *Int. J. Radiat. Oncol. Biol. Phys.* **95**, 149–153 (2016), `https://doi.org/10.1016/j.ijrobp.2016.02.030`.
17. S. Safai, C. Bula, D. Meer and E. Pedroni, *Transl. Cancer Res.* **1**, No. 3 (AME Publishing Company, 2012), `https://doi.org/10.3978/j.issn.2218-676X.2012.10.08`.
18. E. Pedroni, R. Bearpark, T. Böhringer, A. Coray, J. Duppich, S. Forss, D. George, M. Grossmann, G. Goitein, C. Hilbes *et al.*, *Z. Med. Phys.* **14**, 25–34 (2004), `https://doi.org/10.1078/0939-3889-00194`.
19. E. Pearson, O. de Wilde, R. Doyen, E. Forton, Y. Jongen, G. Krier, D. Neuveglise and S. Zaremba, *IEEE Trans. Appl. Supercond.* **24**, 1–4 (2013), `https://doi.org/10.1109/TASC.2013.2284719`.

20. U. Amaldi, N. Alharbi, P. Riboni, M. Karppinen, D. Perini, G. Le Godec, D. Aguglia, D. Tommasini, E. Ravaioli, V. Ferrentino *et al.*, *SIGRUM-A superconducting ion gantry with Riboni's unconventional mechanics* (2021).
21. L. Bottura, E. Felcini, G. De Rijk and B. Dutoit, *Nucl. Instrum. Methods Phys. Res. A* **983**, 164588 (2020), `https://doi.org/10.1016/j.nima.2020.164588`.
22. K. P. Nesteruk, A. Bolsi, A. J. Lomax, D. Meer, S. Van De Water and J. M. Schippers, *Phys. Med. Biol.* **66**, 055018 (2021), `https://doi.org/10.1088/1361-6560/abe02b`.
23. Y.-C. Liao, X. Liu, W. Wang, Z.-Y. Yang, Q.-S. Chen and B. Qin, *Nucl. Sci. Tech.* **35**, 1–11 (2024), `https://doi.org/10.1007/s41365-024-01522-1`.
24. P. Ferracin, G. Ambrosio, M. Anerella, D. Arbelaez, L. Brouwer, E. Barzi, L. D. Cooley, J. Cozzolino, L. G. Fajardo, R. Gupta *et al.*, *IEEE Trans. Appl. Supercond.* **33**, 1–7 (2023), `https://doi.org/10.1109/TASC.2023.3250382`.
25. W. Yang, Y. Zhu, L. Ma, Y. Lei, W. You, Y. Liang, W. Peng, X. Zhu and J. Shi, *IEEE Trans. Appl. Supercond.* **34**, 1–5 (2024), `https://doi.org/10.1109/TASC.2023.3349259`.
26. B. Qin, K. Fan and M. Fan, Fast scanning beamline design applied to proton therapy system based on superconducting cyclotrons, in *Proc. 21th Int. Conf. Cyclotrons Their Appl.* (CERN, Geneva, 2016), `https://doi.org/10.18429/JACoW-Cyclotrons2016-MOP12`.
27. B. Qin, W. Chen, X. Liu, Z. K. Liang, X. Y. Fang, Q. S. Chen, K. F. Liu, J. Yang, D. Li, P. Tan *et al.*, *Proc. IPAC 2017*, `https://doi.org/10.18429/JACoW-IPAC2017-THPVA112` (2017).
28. A. Gabard, M. Negrazus, V. Vrankovic and D. George, *IEEE Trans. Appl. Supercond.* **20**, 794–797 (2010), `https://doi.org/10.1109/TASC.2010.2040916`.
29. W. Chen, B. Qin, X. Fang, Q. Chen, J. Yang and K. Liu, *IEEE Trans. Appl. Supercond.* **28**, 1–4 (2017), `https://doi.org/10.1109/TASC.2017.2775579`.
30. J. Wu, H.-W. Du, S. Xue, J.-Z. Pan, Y.-F. Du and Y.-W. Long, *Nucl. Sci. Tech.* **26**, 040201 (2015), `https://doi.org/10.1007/s41365-017-0273-0`.
31. R. Lopez and J. R. Anglada, *Phys. Rev. Accel. Beams* **23**, 072401 (2020), `https://doi.org/10.1103/PhysRevAccelBeams.23.072401`.
32. F. Regis, P. Manil, P. Fessia, M. Bajko and G. de Rijk, *IEEE Trans. Appl. Supercond.* **20**, 204–207 (2010), `https://doi.org/10.1109/TASC.2010.2043083`.
33. Y. Chen, B. Qin, X. Liu, W. Wang and Y. Liao, *Nucl. Eng. Technol.* **56**, 4365–4374 (2024), `https://doi.org/10.1016/j.net.2024.05.041`.
34. B. Qin, W. Chen, X. Liu, K. Liu, J. Yang, Z. Liang, Q. Chen, X. Fang, Z. Zhao, P. Tan *et al.*, *IEEE Trans. Appl. Supercond.* **28**, 1–5 (2017), `https://doi.org/10.1109/TASC.2017.2772868`.
35. Vector Fields Ltd., *Opera User Guide* (Oxford, 2004).
36. J. T. Tanabe, *Iron Dominated Electromagnets: Design, Fabrication, Assembly and Measurements* (World Scientific, Singapore, 2005).
37. H.-J. Zeng, H.-J. Yao, S.-X. Zheng, X.-L. Guan, X.-W. Wang, P.-F. Ma and H. Ning, *J. Phys. Conf. Ser.* **1067**, 062005 (2018), `https://doi.org/10.1088/1742-6596/1067/6/062005`.
38. Q. Li, W. Kang, X.-J. Sun, C.-D. Deng and W. Chen, *High Power Laser Part. Beams* **29**, 085105-1–085105-5 (2017), `https://doi.org/10.11884/HPLPB201729.170257`.
39. Y.-S. Zhu, M. Yang, Z. Zhang, W. Chen, B.-G. Yin, C.-T. Shi and W. Kang, *Chin. Phys. C* **35**, 684–688 (2011), `https://doi.org/10.1088/1674-1137/35/7/015`.
40. K. Halbach, *Nucl. Instrum. Methods* **74**, 147–164 (1969), `https://doi.org/10.1016/0029-554X(69)90502-3`.